

# Physical Properties of Mn<sub>3</sub>O<sub>4</sub> Nanoparticles One-Step Synthesized at Room Temperature and Short Time

Frank R. Sánchez-Monteza<sup>a</sup>, Segundo R. Jáuregui-Rosas<sup>b,\*</sup>, Olga V. Soledad Flores<sup>c</sup>

<sup>a</sup>Escuela de Física, GMIN-UNT, Universidad Nacional de Trujillo, Trujillo 13011, Perú

<sup>b</sup>Departamento de Física, GMIN-UNT, Universidad Nacional de Trujillo, Trujillo 13011, Perú

<sup>c</sup>Department of Physics, University of Puerto Rico – Mayagüez Campus, 00682, PR  
[sjauregui@unitru.edu.pe](mailto:sjauregui@unitru.edu.pe)

The one-step synthesis of Mn<sub>3</sub>O<sub>4</sub> nanoparticles at room temperature, without additional downstream processes, was carried out by reacting a solution of MnCl<sub>2</sub> in water or alcohol with NaOH at different concentrations for 30 min. Spherical nanoparticles with sizes ranging from 30 to 54 nm were obtained. The characterization by XRD, Raman spectroscopy, and FTIR confirmed the spinel structure of Mn<sub>3</sub>O<sub>4</sub>. UV-VIS spectroscopy allowed to obtain the band gap, ranging from 2.37 to 2.89 eV. Photoluminescence spectroscopy gave evidence of multiple emission bands attributed mainly to structural defects. A greater influence of the type of solvent was observed than that of the NaOH concentration.

## 1. Introduction

In recent decades, nanoscience and nanotechnology have advanced significantly, driven by improvements in synthesis methods and the search for innovative applications. Nanomaterials stand out for their unique properties derived from their small size, which depend on factors such as morphology, size, crystalline structure, and composition. Therefore, precise control of synthesis is key to ensuring both the desired properties and reproducibility. Manganese oxides have been widely investigated for their applications in supercapacitors, batteries (Hou et al., 2022; Raj et al., 2019), catalysis, sensors (Sisakhtnezhad et al., 2023), OLED technologies (Mandal & Choudhary, 2022), medicine (Mahmood et al., 2023; M. R. Shaik et al., 2021), and drug delivery (Chauhan et al., 2023; Mohammad et al., 2023). Among them, Mn<sub>3</sub>O<sub>4</sub> stands out for its stability, low cost, non-toxicity, and ease of synthesis. Although various methods exist for its production, many require complex and time-consuming processes. Although Mn<sub>3</sub>O<sub>4</sub> nanoparticles have been extensively investigated, most reported synthesis routes rely on hydrothermal treatments, elevated temperatures (60 - 120 °C), long reaction times (9 - 24 h), or additional thermal treatments at high temperatures (300 - 500 °C) (Balamurugan et al., 2022; Dhaouadi et al., 2010; Toufiq et al., 2014). In contrast, the present work introduces a simple, fast, and reproducible one-step coprecipitation synthesis carried out at room temperature with a short reaction time of 30 min.

The ability to control crystallite size, band gap, and defect-related emissions through solvent selection makes this synthesis strategy particularly relevant for applications in catalysis, optoelectronic devices, and energy-related systems, where low-cost and scalable production routes are required.

In this study, the combined effect of NaOH concentration and solvent nature on the structural and optical properties of Mn<sub>3</sub>O<sub>4</sub> nanoparticles under mild conditions is evaluated. This approach provides insight into property tunability without thermal treatments, offering a practical and scalable alternative to conventional synthesis methods.

## 2. Methodology

### 2.1 Synthesis of Nanoparticles

Two experimental variants were carried out using 96% ethanol and double-distilled water as solvents. The reagents employed were  $\text{MnCl}_2 \cdot 4\text{H}_2\text{O}$  and  $\text{NaOH}$  (Merck), with purities of 99.9% and 99%, respectively. The reagent amounts were calculated for a total solvent volume of 50 mL. The nanoparticles were synthesized via a one-step coprecipitation method at room temperature ( $T = 20^\circ\text{C}$ ), with an aging time of 30 min and without any post-synthesis thermal treatment. The resulting precipitate was washed three times with double-distilled water, and the samples were dried in an oven at  $70^\circ\text{C}$  for 12 h. Finally, the material was homogenized in an agate mortar. Figure 1 shows a schematic representation of the experimental process.

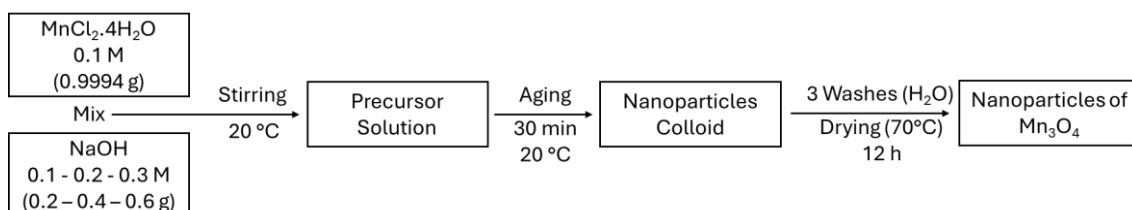


Figure 1: Schematic of  $\text{Mn}_3\text{O}_4$  nanoparticle synthesis

### 2.2 Nanoparticles Characterization

The crystal structure was analyzed by X-ray diffraction using a Rigaku Miniflex600 diffractometer ( $\lambda = 0.154\text{ nm}$ ,  $2\theta$  range:  $15\text{--}70^\circ$ , scan rate:  $2^\circ/\text{min}$ , and step of  $0.02^\circ$ ), and the VESTA software was employed to simulate the crystal structure and generate a theoretical diffraction pattern for comparison. FTIR spectra were acquired using a Perkin Elmer Spectrum Two spectrometer. Raman analysis was conducted with a WITec Alpha 300R confocal Raman microscope equipped with a 532 nm laser. Diffuse reflectance spectra were measured using a Perkin Elmer Lambda 750 UV-vis-NIR spectrometer with a 60 mm Spectralon integrating sphere. Photoluminescence spectra were recorded with a Perkin Elmer LS55 spectrofluorometer using an excitation wavelength of 380 nm. Additionally, the morphology of the nanoparticles was examined using a Thermo Scientific Scios 2 Dual Beam scanning electron microscope.

## 3. Results and analysis

### 3.1 X-ray diffraction

The X-ray diffractograms of nanoparticles synthesized using water and alcohol (Figure 2) show the characteristic diffraction peaks of  $\text{Mn}_3\text{O}_4$ , confirming the formation of a tetragonal structure with the I-41/amd space group. The VESTA simulation (Figure 2(b)) was used to visualize the  $\text{Mn}_3\text{O}_4$  crystal structure, which is a normal spinel with  $\text{Mn}^{2+}$  and  $\text{Mn}^{3+}$  ions occupying tetrahedral and octahedral sites, respectively.

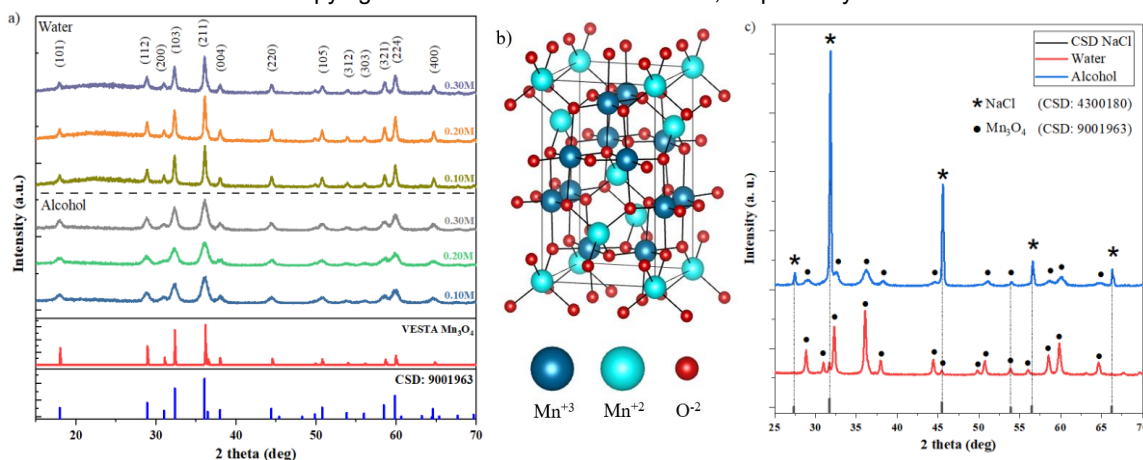


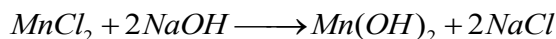
Figure 2: (a) X-ray diffraction (XRD) patterns of  $\text{Mn}_3\text{O}_4$  nanoparticles synthesized in aqueous and alcoholic media; (b) simulated crystal structure of  $\text{Mn}_3\text{O}_4$  generated using VESTA software; (c) XRD patterns of  $\text{Mn}_3\text{O}_4$  nanoparticles synthesized in aqueous and alcoholic media with 0.20 M NaOH, before washing.

This structural model facilitated the generation of a theoretical diffraction pattern, which was subsequently compared with experimental diffractograms and Cambridge Structural Database (CSD) reference data (CSD:9001963). The analysis confirms a single crystalline phase, with no detectable secondary phases or synthesis residues. The average lattice parameters calculated for the samples synthesized in water were  $a = b = 0.5760$  nm and  $c = 0.9530$  nm. In contrast, those synthesized in alcohol exhibited parameters  $a = b = 0.5766$  nm and  $c = 0.9601$  nm; these parameters are similar to those reported by other authors, as is the diffraction pattern (Bose et al., 2021; Bussamara et al., 2013). The most intense peak (211) in Figure 2(a) was used to estimate the lattice parameters, crystallite size using the Scherrer equation, dislocation density, and crystalline strain. The corresponding results are summarized in Table 1.

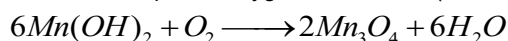
Table 1: Crystallographic parameters of  $Mn_3O_4$  nanoparticles

Solvent	NaOH Molarity (M)	D (nm)	$d_{hkl}$ (nm)	$\delta \times 10^{14}$ (lines/m <sup>2</sup> )	$\epsilon$	$a = b$ (nm)	$c$ (nm)
Water	0.10	23.94	0.2486	17.45	0.26	0.5761	0.9492
	0.20	25.41	0.2486	15.48	0.25	0.5760	0.9496
	0.30	20.75	0.2487	23.22	0.31	0.5762	0.9529
	0.10	9.68	0.2488	106.69	0.66	0.5766	0.9613
Alcohol	0.20	9.01	0.2487	123.29	0.70	0.5762	0.9567
	0.30	10.67	0.2487	87.83	0.59	0.5764	0.9559

Crystalline strain ( $\epsilon = \beta/4\tan\theta$ ) indicates the structural order of the material: low values reflect a well-ordered and stable lattice, while high values indicate defects and internal stresses. In the samples synthesized in water, with crystallite sizes between 20 and 25 nm, the lower crystalline strain value confirms adequate crystal formation, with minimal lattice distortions and good atomic order (Moestopo et al., 2023), consistent with the dislocation density ( $\delta = 1/D^2$ ) values obtained. Conversely, the samples synthesized in alcohol exhibit significantly smaller crystallite sizes, between 9 and 11 nm, but greater crystalline strain, indicating poorer crystallization and a higher density of structural defects. The presence of NaOH during synthesis influences the crystallite size, interplanar spacing, and lattice parameters of the nanoparticles obtained. The size variations among samples synthesized with different solvents may be related to the formation of NaCl during the reaction between manganese chloride and sodium hydroxide.

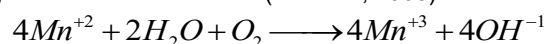


In this first stage,  $Mn^{+2}$  ions react with  $2OH^{-1}$  groups to form manganese hydroxide  $Mn(OH)_2$ . The  $Mn(OH)_2$  molecules are oxidized to  $Mn_3O_4$  while atmospheric oxygen is reduced. (Dhaouadi et al., 2010)



When NaCl is formed in an aqueous medium, it remains dissolved in water and does not crystallize; in contrast, when it is formed in an alcoholic medium, NaCl does not dissolve due to its low or nearly negligible solubility in alcohol, leading to the formation of salt crystals. This behavior is evidenced in Figure 2(c), where the presence of NaCl is significant after recovery of the solid products from the synthesis and removal of the liquid phase. Consequently, the formation of NaCl in an alcoholic medium may contribute to limiting crystallite growth by promoting aggregation and localized nucleation processes. Although this mechanism is consistent with the observed size reduction, further studies are required to directly confirm the role of NaCl during nanoparticle growth. A comparison of samples synthesized at identical NaOH concentrations reveals that changing the solvent from water to alcohol reduces crystallite size by approximately 50 - 60%, whereas variations in NaOH concentration within the same solvent produce comparatively smaller changes, for synthesis in water 12% and in alcohol 11% on average. This quantitative trend supports the conclusion that solvent nature plays a dominant role over alkaline concentration in controlling crystallite growth.

Hu et al. propose that the coexistence of  $Mn^{+2}$  and  $Mn^{+3}$  favors the formation of  $Mn_3O_4$ ; the reduction of divalent manganese to trivalent manganese occurs as follows (Hu et al., 2008):



Leaving as a result a solution rich in  $Mn^{+2}$  and  $Mn^{+3}$  ions, giving way to the formation of  $Mn_3O_4$ .

### 3.2 FT-IR and Raman Spectroscopy

Figure 3 (a) shows the FTIR spectra of the synthesized nanoparticles. The bands found are consistent with those previously reported by other authors (Balamurugan et al., 2022; Mohamed et al., 2022; Sackey et al., 2021). The lower band around  $403\text{ cm}^{-1}$  and the  $476\text{ cm}^{-1}$  band are associated with the asymmetric distortion vibration and the narrowing mode of  $Mn^{+3}$ -O ions in octahedral sites, respectively; the  $593\text{ cm}^{-1}$  band is attributed

to the coupling of bond narrowing modes, bending vibrations of  $\text{Mn}^{2+}\text{-O}$  in tetrahedral sites, and distortion vibrations in octahedral sites of  $\text{Mn}^{3+}\text{-O}$  bonds. The bands in the range  $1070 - 1115 \text{ cm}^{-1}$  present in the samples synthesized in water are attributed to the  $\text{OH}^{-1}$  vibration indicator of the  $\text{Mn}_3\text{O}_4 \rightarrow \gamma\text{-MnO(OH)}$  transformation (Ristić et al., 2013). However, this residue has not been detected by other characterization techniques, indicating that its concentration is likely low. Figure 3 (b) shows the Raman spectra of the nanoparticles, which exhibit the characteristic peaks of  $\text{Mn}_3\text{O}_4$  corresponding to the  $E_g$ ,  $T_{2g}$ , and  $A_{1g}$  vibrational modes, around  $318 \text{ cm}^{-1}$ ,  $372 \text{ cm}^{-1}$ , and  $658 \text{ cm}^{-1}$ , respectively. No signs of impurities are observed, confirming the purity of the material. The  $A_{1g}$  band corresponds to the vibrations of the  $\text{Mn}^{2+}$  ions in tetrahedral coordination. The  $E_g$  and  $T_{2g}$  bands are attributed to the combined vibrations of the tetrahedral and octahedral oxygen atoms. In particles, the Mn-O bending modes and the asymmetric narrowing of the oxygen bridge between manganese (Mn-O-Mn) are observed. The Raman shift ( $\Delta R$ ) values of the samples from lower to higher NaOH concentrations are consistent with reports from other authors (Deka et al., 2024; Diallo et al., 2021; Lan et al., 2019; Vignesh et al., 2021).

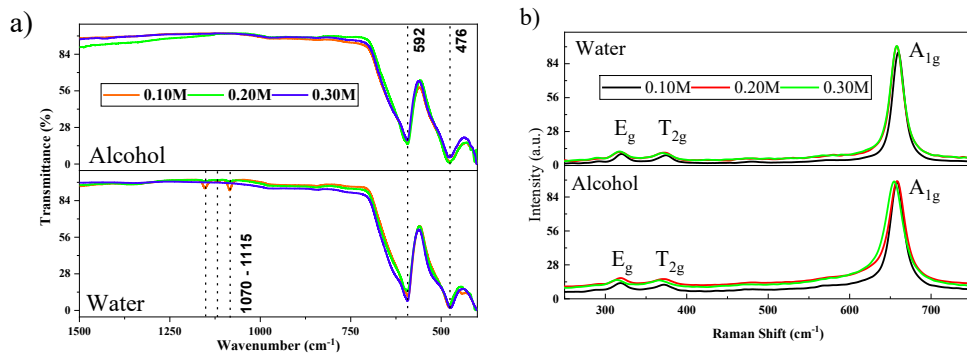


Figure 3: (a) FTIR and (b) Raman spectra of  $\text{Mn}_3\text{O}_4$  nanoparticles synthesized in water and alcohol.

### 3.3 UV-Vis Spectroscopy and Photoluminescence Spectroscopy

From the UV-VIS reflectance spectra, after applying the Kubelka-Munk function and the Tauc method (Figure 4.a), the band gap of the nanoparticles was determined. The band gap of bulk  $\text{Mn}_3\text{O}_4$  is  $2.30 \text{ eV}$ ; the estimated values exceed this value, which may be mainly due to quantum confinement. Other authors report band gap values ranging from  $2.37$  to  $2.89 \text{ eV}$ . (Jarvin et al., 2021; D. P. M. D. Shaik et al., 2019; Vignesh et al., 2021). The photoluminescence spectra in Figure 4.b, obtained under excitation at  $380 \text{ nm}$ , presents five emission bands at  $460$ ,  $490$ ,  $519$ ,  $541$ , and  $589 \text{ nm}$ , with the most prominent bands at  $519$  and  $541 \text{ nm}$ , in agreement with what has been reported in other studies. Vignesh et al. and Taufiq et al. attribute the emissions around  $500 - 543 \text{ nm}$  to electronic transitions associated with oxygen vacancies (Toufiq et al., 2014; Vignesh et al., 2021). Balamurugan et al. assign the band near  $585 \text{ nm}$  to d-d transitions of  $\text{Mn}^{3+}$  (Balamurugan et al., 2022).

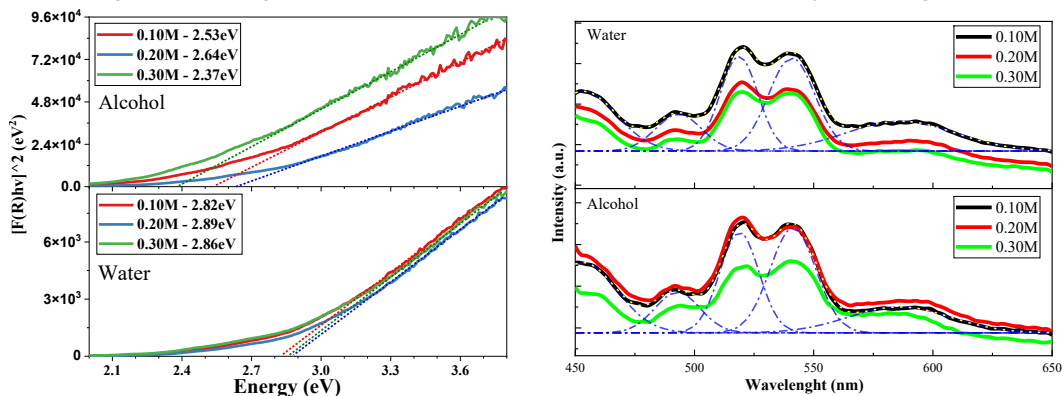


Figure 4: (a) Tauc plot lines obtained from UV-VIS reflectance of the nanoparticles, and (b) photoluminescence spectra of  $\text{Mn}_3\text{O}_4$  nanoparticles synthesized in water and alcohol.

### 3.4 Scanning Electron Microscopy

Figure 5 presents representative SEM images of  $\text{Mn}_3\text{O}_4$  nanoparticles synthesized at NaOH concentrations of  $0.10 \text{ M}$ ,  $0.20 \text{ M}$ , and  $0.30 \text{ M}$  using water and alcohol as solvents. In all cases, the nanoparticles exhibit an approximately spherical morphology. For samples synthesized in water, the average particle sizes are  $47$ ,  $54$ , and  $46 \text{ nm}$ , respectively, whereas those synthesized in alcohol show significantly smaller average sizes of  $33$ ,

30, and 31 nm. At identical NaOH concentrations, the use of alcohol as a solvent lead to a particle size reduction of approximately 30 - 45% compared to water, and between NaOH concentrations the average variation for alcohol is 7% and for water is 14%, indicating that the nature of the solvent plays a dominant role in controlling particle growth. In addition, nanoparticles synthesized in aqueous medium display a more uniform and well-defined morphology, while those obtained in alcohol exhibit increased surface roughness and agglomeration, consistent with the higher crystalline strain observed in XRD analysis.

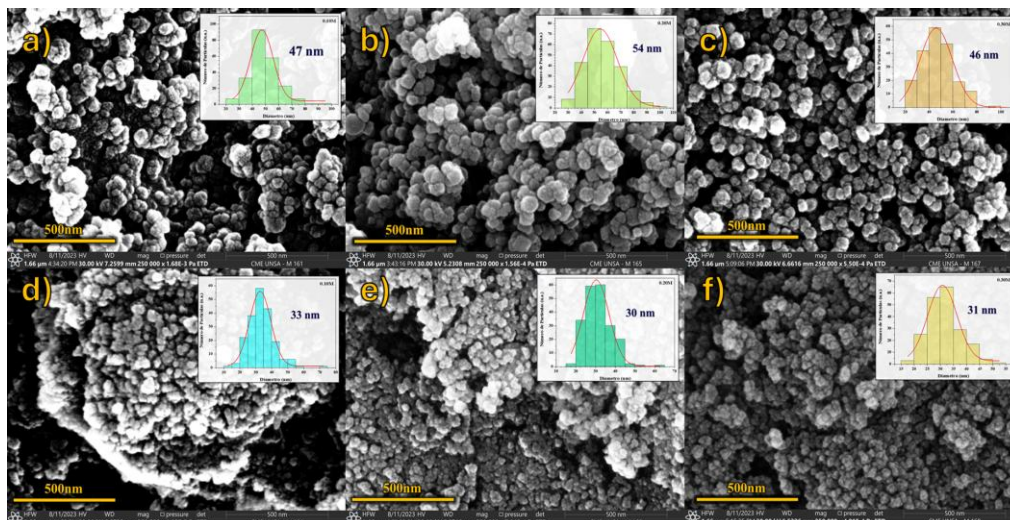


Figure 5: SEM images of  $Mn_3O_4$  nanoparticles, a) 0.10 M, b) 0.20 M, and 0.30 M synthesized in water; d) 0.10 M, e) 0.20 M, and f) 0.30 M synthesized in alcohol.

#### 4. Conclusions

High-purity spherical  $Mn_3O_4$  nanoparticles with a tetragonal crystal structure were successfully synthesized via a one-step coprecipitation method at room temperature and short reaction time. The nanoparticles exhibit band gap values ranging from 2.37 to 2.89 eV and particle sizes between 33 and 54 nm, depending on the synthesis conditions. A quantitative comparison demonstrates that the solvent nature has a more pronounced influence on crystallite size and optical properties than NaOH concentration. These results highlight solvent selection as a key parameter for tailoring the properties of  $Mn_3O_4$  nanoparticles, enabling tunability through a simple, scalable, low-energy synthesis route suitable for catalytic and energy-related applications.

#### Acknowledgments

The authors thank the Laboratorio de Investigación of the Farmacia y Bioquímica faculty for their support with the FTIR analyses and Mg. Fanny V. Samanamud Moreno for her support in LabMIN-UNT.

#### References

- Balamurugan, M., Sivaprakash, P., Sivakumar, S., Ramachandran, S., & Saravanan, S. (2022). Effect of different precursors on structural and luminescence properties of  $Mn_3O_4$  nanoparticles prepared by coprecipitation method. *Materialwissenschaft Und Werkstofftechnik*, 53(6), 723-731. <https://doi.org/10.1002/mawe.202100299>
- Bose, V. C., Sugathan, N., & Biju, V. (2021). Novel sol-gel method for low temperature synthesis of nanostructured  $Mn_3O_4$ : Structure, cation valence states, optical and electrical properties. *Journal of Crystal Growth*, 555, 125961. <https://doi.org/10.1016/j.jcrysgro.2020.125961>
- Bussamara, R., Melo, W. W. M., Scholten, J. D., Migowski, P., Marin, G., Zapata, M. J. M., Machado, G., Teixeira, S. R., Novak, M. A., & Dupont, J. (2013). Controlled synthesis of  $Mn_3O_4$  nanoparticles in ionic liquids. *Dalton Transactions*, 42(40), 14473-14479. <https://doi.org/10.1039/C3DT32348J>
- Chauhan, S., Solanki, R., Kumar Jangid, A., Jain, P., Pranjali, P., Patel, S., Guleria, A., Pooja, D., & Kulhari, H. (2023). Manganese nanocarrier for matrix metalloproteinase 9 responsive delivery of irinotecan for colon cancer treatment. *Journal of Industrial and Engineering Chemistry*. <https://doi.org/10.1016/j.jiec.2023.07.057>
- Deka, K., Deshpande, G. A., Ghodke, N. P., Fischer, J., Bock, M., Khot, P., Kodam, K. M., & Mathe, V. L. (2024). Thermal plasma synthesized  $Mn_3O_4$  nanoparticles as T1 and T2 MRI contrast agents. *Ceramics International*, 50(17, Part A), 29518-29527. <https://doi.org/10.1016/j.ceramint.2024.05.247>

- Dhaouadi, H., Madani, A., & Touati, F. (2010). Synthesis and spectroscopic investigations of Mn<sub>3</sub>O<sub>4</sub> nanoparticles. *Materials Letters*, 64(21), 2395-2398. <https://doi.org/10.1016/j.matlet.2010.07.036>
- Diallo, A., Tandjigora, N., Ndiaye, S., Jan, T., Ahmad, I., & Maaza, M. (2021). Green synthesis of single phase hausmannite Mn<sub>3</sub>O<sub>4</sub> nanoparticles via *Aspalathus linearis* natural extract. *SN Applied Sciences*, 3(5), 562. <https://doi.org/10.1007/s42452-021-04550-3>
- Hou, J., Li, J., Guo, Y., Xu, Y., Zhang, Y., Fang, Z., Yang, J., & Wu, M. (2022). Nanoparticles constructed mesoporous coral-like Mn<sub>2</sub>O<sub>3</sub> as high-performance anode for lithium-ion batteries. *Ceramics International*, 48(18), 26539-26545. <https://doi.org/10.1016/j.ceramint.2022.05.349>
- Hu, C.-C., Wu, Y.-T., & Chang, K.-H. (2008). Low-Temperature Hydrothermal Synthesis of Mn<sub>3</sub>O<sub>4</sub> and MnOOH Single Crystals: Determinant Influence of Oxidants. *Chemistry of Materials*, 20(9), 2890-2894. <https://doi.org/10.1021/cm703245k>
- Jarvin, M., Kumar, S. A., Vinodkumar, G., Manikandan, E., & Inbanathan, S. S. R. (2021). Enhanced photocatalytic performance of Hausmannite Mn<sub>3</sub>O<sub>4</sub> -rGO nanocomposite in degrading methylene blue. *Materials Letters*, 305, 130750. <https://doi.org/10.1016/j.matlet.2021.130750>
- Lan, D., Qin, M., Yang, R., Wu, H., Jia, Z., Kou, K., Wu, G., Fan, Y., Fu, Q., & Zhang, F. (2019). Synthesis, characterization and microwave transparent properties of Mn<sub>3</sub>O<sub>4</sub> microspheres. *Journal of Materials Science: Materials in Electronics*, 30(9), 8771-8776. <https://doi.org/10.1007/s10854-019-01201-7>
- Mahmood, A., Munir, T., Rasul, A., Ghfar, A. A., & Mumtaz, S. (2023). Polyethylene glycol and chitosan functionalized manganese oxide nanoparticles for antimicrobial and anticancer activities. *Journal of Colloid and Interface Science*, 648, 907-915. <https://doi.org/10.1016/j.jcis.2023.06.029>
- Mandal, G., & Choudhary, R. B. (2022). MnO<sub>2</sub> integrated emeraldine polyaniline (PANI- MnO<sub>2</sub>) nanocomposites with inflated opto-electrical traits as ETLs for OLED applications. *Materials Science in Semiconductor Processing*, 151, 107000. <https://doi.org/10.1016/j.mssp.2022.107000>
- Moestopo, W. P., Shaker, S., Deng, W., & Greer, J. R. (2023). Knots are not for naught: Design, properties, and topology of hierarchical intertwined microarchitected materials. *Science Advances*, 9(10), eade6725. <https://doi.org/10.1126/sciadv.ade6725>
- Mohamed, M. M., Khairy, M., Amer, A. A., & Mousa, M. A. (2022). Nonconventional synthesis of polyhedral Mn<sub>3</sub>O<sub>4</sub> nanoarchitectures incorporated reduced graphene oxide: Superior supercapacitor capabilities. *Journal of Materials Research and Technology*, 21, 2555-2570. <https://doi.org/10.1016/j.jmrt.2022.10.066>
- Mohammad, F., Bwatanglang, I. B., Al-Lohedan, H. A., Shaik, J. P., Moosavi, M., Dahan, W. M., Al-Tilasi, H. H., Aldhayan, D. M., Chavali, M., & Soleiman, A. A. (2023). Magnetically controlled drug delivery and hyperthermia effects of core-shell Cu@Mn<sub>3</sub>O<sub>4</sub> nanoparticles towards cancer cells in vitro. *International Journal of Biological Macromolecules*, 249, 126071. <https://doi.org/10.1016/j.ijbiomac.2023.126071>
- Raj, H., Sil, A., & Pulagara, N. V. (2019). MnO anchored reduced graphene oxide nanocomposite for high energy applications of Li-ion batteries: The insight of charge-discharge process. *Ceramics International*, 45(12), 14829-14841. <https://doi.org/10.1016/j.ceramint.2019.04.214>
- Ristić, M., Musić, S., Popović, S., Dragčević, Đ., Marciuš, M., & Ivanda, M. (2013). Synthesis and long-term phase stability of Mn<sub>3</sub>O<sub>4</sub> nanoparticles. *Journal of Molecular Structure*, 1044, 255-261. <https://doi.org/10.1016/j.molstruc.2012.11.023>
- Sackey, J., Akbari, M., Morad, R., Bashir, A. K. H., Ndiaye, N. M., Matinise, N., & Maaza, M. (2021). Molecular dynamics and biosynthesis of phoenix dactylifera mediated Mn<sub>3</sub>O<sub>4</sub> nanoparticles: Electrochemical application. *Journal of Alloys and Compounds*, 854, 156987. <https://doi.org/10.1016/j.jallcom.2020.156987>
- Shaik, D. P. M. D., Rosaiah, P., & Hussain, O. M. (2019). Fabrication of the Mn<sub>3</sub>O<sub>4</sub> thin film electrodes by electron beam evaporation for supercapacitor applications. *Journal of Electroanalytical Chemistry*, 851, 113409. <https://doi.org/10.1016/j.jelechem.2019.113409>
- Shaik, M. R., Syed, R., Adil, S. F., Kuniyil, M., Khan, M., Alqahtani, M. S., Shaik, J. P., Siddiqui, M. R. H., Al-Warthan, A., Sharaf, M. A. F., Abdelgawad, A., & Awwad, E. M. (2021). Mn<sub>3</sub>O<sub>4</sub> nanoparticles: Synthesis, characterization and their antimicrobial and anticancer activity against A549 and MCF-7 cell lines. *Saudi Journal of Biological Sciences*, 28(2), 1196-1202. <https://doi.org/10.1016/j.sjbs.2020.11.087>
- Sisakhtnezhad, S., Rahimi, M., & Mohammadi, S. (2023). Biomedical applications of MnO<sub>2</sub> nanomaterials as nanozyme-based theranostics. *Biomedicine & Pharmacotherapy*, 163, 114833. <https://doi.org/10.1016/j.biopha.2023.114833>
- Toufiq, A., Wang, F., Javed, D., Qurat ul ain, Li, Q., Yan, L., & Khan, M. (2014). Synthesis, characterization and photoluminescent properties of 3D nanostructures self-assembled with Mn<sub>3</sub>O<sub>4</sub> nanoparticles. *Materials Express*, 4. <https://doi.org/10.1166/mex.2014.1167>
- Vignesh, R., Sivakumar, R., & Sanjeeviraja, C. (2021). A detailed analysis on optical parameters of spinel structured Mn<sub>3</sub>O<sub>4</sub> thin films deposited by nebulized spray pyrolysis technique. *Optical Materials*, 111, 110580. <https://doi.org/10.1016/j.optmat.2020.110580>